Supporting Information for "How do earthquakes stop? Insights from a minimal model of frictional rupture"

Fabian Barras[1], Kjetil Thøgersen[1], Einat Aharonov[1,2], François Renard[1,3]

[1]The Njord Centre, Departments of Geosciences and Physics, box 1048, University of Oslo, Blindern, 0316 Oslo, Norway

[2]Institute of Earth Sciences, The Hebrew University, Jerusalem, 91904, Israel

[3]ISTerre, Univ. Grenoble Alpes, Grenoble INP, Univ. Savoie Mont Blanc, CNRS, IRD, Univ. Gustave Eiffel, 38000, Grenoble, France

The Supporting Information contains a list of main symbols, one table, six figures, and seven supplementary text sections.

List of main symbols

$\bar{x}$	Position along the fault
$\bar{t}$	Time
$\bar{u}$	Slip
$\bar{\tau}$	Shear stress
$\bar{\tau}_f$	Frictional stress
$\bar{\Gamma}$	Boundary conditions: imposed-stress ($\Gamma = 0$) or imposed-displacement ($\Gamma = 1$)
$\bar{\gamma}$	Elastic modulus parameter
$\bar{\tau}_k$	Pre-stress
$\bar{d}_c$	Critical weakening distance
$\bar{G}_c = \bar{d}_c/2$	Fracture energy
$\bar{K}$	One-dimensional stress intensity factor
$\bar{W}_b$	Breakdown work
$\bar{E}_{\text{el}}$	Elastic energy
$\bar{E}_{\text{kin}}$	Kinetic energy
$\bar{W}_{\text{ext}}$	External work
$\bar{v}_c$	Rupture propagation speed
$\bar{u}_p$	Final slip (i.e. after rupture arrest)
$\bar{\beta}$	Numerical damping
$\bar{\mathcal{L}}$	Length of the domain
$\bar{L}$	Rupture length
$\bar{L}_{\text{arr}}$	Arrest length
x	Position
t	Time
u_i	Displacement
$\hat{u}_0$	Imposed displacement at the top boundary
$\langle u_i \rangle$	Average displacement over the block height
σ_{ij}	Cauchy stress tensor
σ_n	Normal stress at the interface
τ_f	Frictional (shear) stress at the interface
H	Height of the solid block
λ	Lamé first coefficient
$\mathcal{G}$	Shear modulus
ρ	Solid density
μ_s	Static friction coefficient
μ_k	Dynamic friction coefficient
d_c	Critical slip weakening distance

S.1. One-dimensional elastodynamic model

Let us consider the linear elastic block and associated system of coordinates presented in Figure 2. For each coordinate ($i = x, y, z$), the balance of linear momentum writes:

$$\rho \frac{\partial^2 u_i}{\partial t^2} = \frac{\partial \sigma_{xi}}{\partial x} + \frac{\partial \sigma_{yi}}{\partial y} + \frac{\partial \sigma_{zi}}{\partial z}, \tag{S.1}$$

where σ_{ij} are the components of the Cauchy stress tensor and u_i is the displacement field. Next, we assume that the normal stress is homogeneous and constant ($\sigma_{yy}(x, y, z, t) \equiv \sigma_n$) and that the elastic fields are invariant in the out-of-plane direction ($\partial u_i/\partial_z = 0$), such that the momentum balance equation becomes

$$\rho \frac{\partial^2 u_i}{\partial t^2} = \Lambda \frac{\partial^2 u_i}{\partial x^2} + \frac{\partial \sigma_{yi}}{\partial y}. \tag{S.2}$$

The equation above applies equivalently to mode II displacement, for which i corresponds to x and $\Lambda = \lambda + 2\mathcal{G}$, and to mode III displacement, for which i corresponds to z and $\Lambda = \mathcal{G}$. The height of the system H is assumed to be small compared to the other dimensions of the problem, such that variations of u_i over y are small and the momentum balance can be solved in average across the height (Bouchbinder et al., 2011; Bar-Sinai et al., 2013). At time $t = 0$, the system is initially at rest, such that one can define the height-averaged displacement field as

$$\langle u_i \rangle_y(x, t) = \frac{1}{H} \int_0^H \Big(u_i(x, y, t) - u_i(x, y, 0) \Big) \mathrm{dy}, \tag{S.3}$$

with $u_i(x, y, 0)$ corresponding to the initial static displacement field. Using the definition of $\langle u_i \rangle_y$, both sides of Eq. (S.2) are integrated between zero and H to obtain the following one-dimensional formulation:

$$H\rho \frac{\partial^2 \langle u_i \rangle_y}{\partial t^2} = H\Lambda \frac{\partial^2 \langle u_i \rangle_y}{\partial x^2} + \sigma_{yi}(x, H, t) - \sigma_{yi}(x, 0, t). \tag{S.4}$$

Next, the boundary conditions on the top and bottom surfaces need to be applied. The shear stress on the bottom surface corresponds to the frictional stress:

$$\sigma_{yi}(x,0,t) \equiv \tau_f(x,t). \tag{S.5}$$

On the top surface, two kinds of boundary conditions can be considered:

$$\text{stress} - \text{controlled} : \sigma_{yi}(x,H,t) \equiv \tau_0(x) \tag{S.6}$$

$$\text{displacement} - \text{controlled} : u_i(x,H,t). \equiv \hat{u}_0(x) \tag{S.7}$$

For imposed stress, the value of the shear stress at the top boundary is fixed, whereas for imposed displacement $\sigma_{yi}(x,H,t)$ evolves with interfacial slip. To estimate this evolution, the displacement field through the height of the block can be expressed as the following Taylor expansion

$$u_i(x,y,t) = u_i(x,H,t) + (y-H)\frac{\partial u_i(x,y,t)}{\partial y}|_{y=H} + \mathcal{O}\Big((y-H)^2\Big). \tag{S.8}$$

In the right-hand side of the equation above, the first term corresponds to the imposed-displacement $\hat{u}_0$, the derivative in the second term corresponds to $\sigma_{yi}(x,H,t)/\mathcal{G}$ and the third term accounts for higher-order contributions that can be neglected as variations of u_i through H are small. Invoking that the initial static displacement field corresponds to $u_i(x,y,0) = \hat{u}_0(x)y/H$, the height-averaged displacement can be integrated following Eq. (S.3) as:

$$\langle u_i \rangle_y(x,t) = \frac{1}{2}\hat{u}_0(x) - \frac{H}{2\mathcal{G}}\sigma_{yi}(x,H,t). \tag{S.9}$$

From the equation above, $\sigma_{yi}(x,H,t)$ can then be expressed as an initial shear stress τ_0 related to the imposed displacement minus the elastic relaxation resulting from slip:

$$\sigma_{yi}(x,H,t) = \frac{\mathcal{G}}{H}\Big(\hat{u}_0(x) - 2\langle u_i \rangle_y(x,t)\Big) \equiv \tau_0(x) - \frac{2\mathcal{G}}{H}\langle u_i \rangle_y(x,t). \tag{S.10}$$

Using Eqs. (S.5), (S.6) and (S.10), the momentum equation (S.4) can be re-written as:

$$\frac{\partial^2\langle u_i\rangle_y}{\partial t^2} = \frac{\Lambda}{\rho}\frac{\partial^2\langle u_i\rangle_y}{\partial x^2} - \Gamma\frac{2\mathcal{G}}{\rho H^2}\langle u_i\rangle_y + \frac{1}{\rho H}\Big(\tau_0(x) - \tau_f(x,t)\Big), \tag{S.11}$$

where Γ is a binary parameter being equal to zero for stress boundary condition, and equal to one for displacement boundary condition on the top surface.

Following the normalization procedure summarized in Table S1, the one-dimensional momentum equation above can be re-written in the dimensionless form:

$$\frac{\partial^2\bar{u}}{\partial\bar{t}^2} = \frac{\partial^2\bar{u}}{\partial\bar{x}^2} - \Gamma\bar{\gamma}\bar{u} + \bar{\tau}, \tag{S.12}$$

which is Eq. (1) in the main text. In Table S1, the dimensionless shear stress is defined with respect to the static μ_s and kinematic μ_k coefficient of friction. For the example of linear slip-weakening friction with only positive slip velocities, the shear stress can be expressed as function of the deviation from residual friction $\bar{\tau}_f$:

$$\bar{\tau}(\bar{x},\bar{t}) = \bar{\tau}_k(\bar{x}) - \bar{\tau}_f(\bar{x},\bar{t}) \begin{cases} > \bar{\tau}_k - 1 & \text{, if } \ \dot{\bar{u}} = 0 \\ = \bar{\tau}_k - (1 - \bar{u}/\bar{d}_c) & \text{, if } \ 0 \le \bar{u} \le \bar{d}_c \\ = \bar{\tau}_k & \text{, if } \ \bar{u} > \bar{d}_c \end{cases}, \tag{S.13}$$

with $\bar{d}_c$ being the critical slip distance and $\bar{\tau}_k$ the dimensionless residual friction defined in Eq. (3). Equation (S.13) also describes Amontons-Coulomb friction in the limit $\bar{d}_c = 0$.

S.2. Parameters and convergence of the numerical scheme

As described in Section 3 of the main text, the one-dimensional model is solved in space using a central finite-difference scheme with uniform grid size $\Delta\bar{x}$ and integrated in time following Euler-Cromer scheme (Cromer, 1981), with uniform time step $\Delta\bar{t}$. At time step j and element i, the integration of a slipping portion of the interface writes

$$\begin{cases} \ddot{\bar{u}}_i^j = \dfrac{\bar{u}_{i+1}^j - 2\bar{u}_i^j + \bar{u}_{i-1}^j}{(\Delta\bar{x})^2} - \Gamma\bar{\gamma}\bar{u}_i^j + \bar{\tau}_i + \bar{\beta}\dfrac{\dot{\bar{u}}_{i+1}^j - 2\dot{\bar{u}}_i^j + \dot{\bar{u}}_{i-1}^j}{(\Delta\bar{x})^2}, \\ \dot{\bar{u}}_i^{j+1} = \dot{\bar{u}}_i^j + \ddot{\bar{u}}_i^j \Delta\bar{t}, \\ \bar{u}_i^{j+1} = \bar{u}_i^j + \dot{\bar{u}}_i^{j+1}\Delta\bar{t}. \end{cases} \tag{S.14}$$

The one-dimensional model in its discretized model (S.14) is similar to the dynamics of Burridge-Knopoff models whose governing equation has the generic form:

$$m\ddot{u} - k(u_{i+1} - 2u_i + u_{i-1}) + lu_i - \eta(\dot{u}_{i+1} - 2\dot{u}_i + \dot{u}_{i-1}^k) = f_i, \tag{S.15}$$

with m being the mass of the block, k, l respectively the longitudinal and leaf spring constants and f_i the driving force. As described by Knopoff and Ni (2001), at the tip of a propagating rupture, the moving boundary between sticking and slipping portion of the fault creates numerical oscillations that can be removed by introducing a viscous damping term η. A spectral analysis of Eq. (S.15) shows that setting $\eta = \sqrt{km}$ implies that the spurious oscillations with grid-size wavelength are critically damped (Amundsen et al., 2012). In practice, Burridge-Knopoff models typically use a value of $\eta = \sqrt{0.1km}$ which provides the best compromise between reducing the numerical oscillations and not damping the physical rupture dynamics (Knopoff & Ni, 2001; Amundsen et al., 2012).

This value is adopted in our one-dimensional simulations with Amontons-Coulomb friction law. Using the analogy between Eqs. (S.14) and (S.15), this corresponds to $m = 1$, $k = (\Delta\bar{x})^{-2}$ and $\beta = \eta(\Delta\bar{x})^2 = \sqrt{0.1km}(\Delta\bar{x})^2 = \sqrt{0.1}\Delta\bar{x}$. This relative viscous damping

term reduces the convergence rate from quadratic to linear but guarantees the stability of the numerical scheme for discontinuous problems as shown in Figure S1. $\Delta\bar{x} \leq 4 \cdot 10^{-3}$ together with the Courant-Friedrichs–Lewy condition (Courant et al., 1928), $\Delta\bar{t} \leq 0.1\Delta\bar{x}$, have been adopted in the simulations reported in the present study to guarantee the numerical convergence.

S.3. Pulse equations

The pulse equation can be expressed by integrating the total energy between the nucleation position $\bar{x} = 0$ and the position of the leading head of the pulse $\bar{L}(\bar{t})$ at time $\bar{t}$ using Eqs. (12) to (14). Next, we assume that the width of the pulse is much smaller than the total ruptured length. This assumption allows us 1) to neglect the contribution of the kinetic energy which is only non-zero within the pulse and 2) to substitute $\bar{u}(\bar{x}, \bar{t})$ by the final slip $\bar{u}_p(\bar{x})$ observed in the wake of the pulse. The total energy at time $\bar{t}$ writes then:

$$\bar{E}(\bar{t}) = \int_0^{\bar{L}(\bar{t})} \left\{ \bar{\tau}_k \bar{u}_p - \bar{W}_b - \frac{1}{2}\Big(\frac{\partial \bar{u}_p}{\partial \bar{x}}\Big)^2 - \frac{1}{2}\bar{\gamma}\bar{u}_p^2 \right\} \mathrm{d}\bar{x}. \tag{S.16}$$

We next use integration by parts and the fact that $\bar{u}_p$ is zero at the two bounds of the integral above to rewrite the equation as:

$$\bar{E}(\bar{t}) = \int_0^{\bar{L}(\bar{t})} \left\{ \bar{\tau}_k \bar{u}_p - \bar{W}_b + \frac{1}{2}\bar{u}_p \frac{\partial^2 \bar{u}_p}{\partial \bar{x}^2} - \frac{1}{2}\bar{\gamma}\bar{u}_p^2 \right\} \mathrm{d}\bar{x} \tag{S.17}$$

Finally, the total energy should be conserved throughout pulse propagation, which implies that:

$$\frac{\mathrm{d}\bar{E}}{\mathrm{d}\bar{L}} = 0 = \bar{\tau}_k \bar{u}_p - \bar{W}_b + \frac{1}{2}\bar{u}_p \frac{\partial^2 \bar{u}_p}{\partial \bar{x}^2} - \frac{1}{2}\bar{\gamma}\bar{u}_p^2. \tag{S.18}$$

This pulse equation can be used to predict the final slip observed in the wake of pulse-like rupture as function of the profile of shear stress lumped in $\bar{\tau}_k(\bar{x})$ and the interface breakdown energy described by $\bar{W}_b$.

S.3.1. Amontons-Coulomb friction

With Amontons-Coulomb friction, the breakdown work is negligible ($\bar{W}_b = 0$). Excluding the trivial solution $\bar{u}_p = 0$, the final slip is given by the following second-order linear pulse equation:

$$\frac{\partial^2 \bar{u}_p}{\partial \bar{x}^2} = \bar{\gamma}\bar{u}_p - 2\bar{\tau}_k. \tag{S.19}$$

This pulse equation can be used for example to predict how $\bar{u}_p$ decays within a stress barrier by defining the initial value problem $u_p(\bar{x}' = 0) = 2\tau_{k,0}/\bar{\gamma}$ with $\bar{x}' = \bar{x} - \bar{x}_b$, which has a general solution given by two constants C_1 and C_2:

$$\bar{u}_p(\bar{x}') = \frac{2\bar{\tau}_{k,b}}{\bar{\gamma}} + C_1 \exp(-\bar{x}'\sqrt{\bar{\gamma}}) + C_2 \exp(\bar{x}'\sqrt{\bar{\gamma}}). \tag{S.20}$$

Neglecting the growing exponential C_2, the following exponential decay can be predicted

$$\bar{u}_p(\bar{x}') = \frac{2}{\bar{\gamma}}\Big(\bar{\tau}_{k,b} + (\bar{\tau}_{k,0} - \bar{\tau}_{k,b}) \exp(-\bar{x}'\sqrt{\bar{\gamma}})\Big). \tag{S.21}$$

Remembering that in the case of stress barrier $\bar{\tau}_{k,b} < 0$, the equation above has a positive root $\bar{u}_p(\bar{x}' = \bar{L}_{\text{arr}}) = 0$ which can be used to predict the critical barrier length:

$$\bar{L}_{\text{arr}} = \bar{\gamma}^{-\frac{1}{2}} \ln\Big(\frac{\bar{\tau}_{k,0} - \bar{\tau}_{k,b}}{-\bar{\tau}_{k,b}}\Big). \tag{S.22}$$

Another prediction can be made by searching C_1 and C_2 such that both $\bar{u}_p(\bar{x}')$ and its first derivative are zero at $\bar{x}' = \bar{L}_{\text{arr}}$ and corresponds to:

$$\bar{u}_p(\bar{x}') = \frac{-2\bar{\tau}_{k,b}}{\bar{\gamma}}\Big(\cosh\Big((\bar{x}' - \bar{L}_{\text{arr}})\sqrt{\bar{\gamma}}\Big) - 1\Big). \tag{S.23}$$

In such case, the theoretical prediction of the arrest length becomes

$$\bar{L}_{\text{arr}} = \bar{\gamma}^{-\frac{1}{2}} \text{arccosh}\Big(\frac{\bar{\tau}_{k,0} - \bar{\tau}_{k,b}}{-\bar{\tau}_{k,b}}\Big). \tag{S.24}$$

The two predictions (S.21) and (S.23) are compared to the the slip profile obtained from numerical simulation in Figure S2.

S.3.2. Slip-weakening friction with $\bar{u}_p \leq \bar{d}_c$

Such case describes frictional weakening which does not reach a residual value. The breakdown work depends on the final slip $\bar{u}_p$

$$\bar{W}_b(\bar{u}_p) = \int_0^{\bar{u}_p} \bar{\tau}_f(\bar{u})\,\mathrm{d}\bar{u} = \int_0^{\bar{u}_p} (1 - \frac{\bar{u}}{d_c})\,\mathrm{d}\bar{u} = \bar{u}_p\Big(1 - \frac{\bar{u}_p}{2\bar{d}_c}\Big), \tag{S.25}$$

and leads to a similar pulse equation:

$$\frac{\partial^2 \bar{u}_p}{\partial \bar{x}^2} = \Big(\bar{\gamma} - \frac{1}{\bar{d}_c}\Big)\bar{u}_p - 2(\bar{\tau}_k - 1). \tag{S.26}$$

S.3.3. Slip-weakening friction with $\bar{u}_p > \bar{d}_c$

If one assumes that frictional weakening and associated breakdown work reach constant values ($\bar{W}_b = \bar{d}_c/2$), the pulse equation becomes non-linear:

$$\frac{\partial^2 \bar{u}_p}{\partial \bar{x}^2} = \bar{\gamma}\bar{u}_p - 2\bar{\tau}_k + \frac{\bar{d}_c}{\bar{u}_p}. \tag{S.27}$$

S.3.4. Steady-state energy balance

Thøgersen, Aharonov, Barras, and Renard (2021) derived the steady-state pulse solution for Amontons-Coulomb friction and homogeneous stress condition. The steady-state pulse has a width

$$\bar{\omega} = \pi\sqrt{\frac{\bar{v}_c^2 - 1}{\bar{\gamma}}} = \frac{\pi\bar{\tau}_k}{\sqrt{\bar{\gamma}(1 - \bar{\tau}_k^2)}} \tag{S.28}$$

over which the slip evolves as

$$\bar{u}(\bar{\xi}) = \frac{\bar{\tau}_k}{\bar{\gamma}}\Big(1 - \sin(\pi\bar{\xi}/\bar{\omega})\Big), \tag{S.29}$$

with $\bar{\xi} \in [-\bar{\omega}/2, \bar{\omega}/2]$ being a co-moving frame of reference centered at the position of peak slip velocity. Integrating the steady state solution between $-\bar{\omega}/2$ and $\bar{\omega}/2$ following Eqs. (12) and (13), one can compute the mechanical (reversible) energy stored within the

steadily travelling pulse:

$$E_{\text{pulse}} = \frac{1}{2}\int_{-\bar{\omega}/2}^{\bar{\omega}/2} \left\{ \left(\frac{\partial \bar{u}}{\partial \bar{x}}\right)^2 + \bar{\gamma}\bar{u}^2 + \left(\frac{\partial \bar{u}}{\partial \bar{t}}\right)^2 \right\} d\bar{x} = \frac{\pi \bar{\tau}_k (1+\bar{\tau}_k^2)}{2\bar{\gamma}^{3/2}\sqrt{1-\bar{\tau}_k^2}}. \tag{S.30}$$

S.4. Crack equations

S.4.1. Steady-state solution under homogeneous stress conditions

A crack-like rupture involves different energy transfer than the pulse-like rupture discussed in the previous section. To complement the steady-state pulse solution (S.29) from Thøgersen et al. (2021), we derive hereafter an equivalent self-similar crack solution under homogeneous prestress $\bar{\tau}_k$. Figure S3 presents three different simulations of crack-like rupture ($\Gamma = 0$) under three different homogeneous pre-stress conditions. Under such conditions, the crack reaches constant propagation speed such that, in the co-moving frame $\bar{\zeta} = \bar{x}/\bar{L}$, self-similar profiles are observed for the acceleration $\ddot{\bar{u}}$, the rescaled velocity $\dot{\bar{u}}\,\bar{t}^{-1}$ and the rescaled displacement $\bar{u}\,\bar{t}^{-2}$. From these results, one can postulate the following self-similar solution:

$$\begin{aligned} \bar{u} &= \bar{t}^{\,2}\mathcal{F}(\bar{\zeta}), && \text{with } \bar{\zeta} = \frac{\bar{x}}{\bar{v}_c \bar{t}}, \\ \dot{\bar{u}} &= \bar{t}\mathcal{H}(\bar{\zeta}), && \text{with } \mathcal{H}(\bar{\zeta}) = 2\mathcal{F}(\bar{\zeta}) - \bar{\zeta}\mathcal{F}'(\bar{\zeta}), \\ \ddot{\bar{u}} &= \mathcal{J}(\bar{\zeta}), && \text{with } \mathcal{J}(\bar{\zeta}) = 2\mathcal{F}(\bar{\zeta}) - 2\bar{\zeta}\mathcal{F}'(\bar{\zeta}) + \bar{\zeta}^2\mathcal{F}''(\bar{\zeta}), \end{aligned} \tag{S.31}$$

where $\mathcal{F}(\bar{\zeta})$ is the self-similar crack displacement solution to be determined. First, this solution needs to satisfy the one-dimensional momentum balance Eq. (1), which becomes in the new frame of reference:

$$2\mathcal{F} - 2\bar{\zeta}\frac{d\mathcal{F}}{d\bar{\zeta}} + (\bar{\zeta}^2 - \frac{1}{\bar{v}_c^2})\frac{d^2\mathcal{F}}{d\bar{\zeta}^2} = \bar{\tau}_k. \tag{S.32}$$

Eq. (S.32) is a Cauchy-Euler equation that reduces to

$$2C - \frac{2A}{\bar{v}_c^2} = \bar{\tau}_k, \tag{S.33}$$

for homogeneous $\bar{\tau}_k$ and if $\mathcal{F}$ has a quadratic form $\mathcal{F} = A\bar{\zeta}^2 + B\bar{\zeta} + C$. A single quadratic solution could not match the simulation profiles, such that the following bi-quadratic solution was postulated:

$$\mathcal{F}(\bar{\zeta}) = \begin{cases} A_1\bar{\zeta}^2 + B_1\bar{\zeta} + C_1, & \text{if } \bar{\zeta} < \bar{\zeta}_c \\ \\ A_2\bar{\zeta}^2 + B_2\bar{\zeta} + C_2, & \text{if } \bar{\zeta} > \bar{\zeta}_c \end{cases} \tag{S.34}$$

Next, the following conditions are imposed

- Zero slip and slip velocity at the fixed boundary on the left of the domain: $\mathcal{F}(\bar{\zeta} = 0) = \mathcal{H}(\bar{\zeta} = 0) = 0$;
- Zero slip and slip velocity at the tip of the crack: $\mathcal{F}(\bar{\zeta} = 1) = \mathcal{H}(\bar{\zeta} = 1) = 0$;
- Continuity of slip and slip velocity at $\bar{\zeta} = \bar{\zeta}_c$;
- The two polynomials should satisfy the momentum balance relationship of Eq. (S.33).

They provide seven conditions to determine the seven unknowns of the self-similar solution which becomes

$$\mathcal{F}(\bar{\zeta}) = \begin{cases} \bar{\tau}_k\bar{v}_c^2\Big(-\dfrac{1}{2}\bar{\zeta}^2 + \dfrac{\bar{\zeta}}{\bar{v}_c + 1}\Big), & \text{if } \bar{\zeta} < \dfrac{1}{\bar{v}_c} \\ \dfrac{\bar{\tau}_k\bar{v}_c^2}{2(\bar{v}_c^2 - 1)}\Big(\bar{\zeta}^2 - 2\bar{\zeta} + 1\Big), & \text{if } \bar{\zeta} > \dfrac{1}{\bar{v}_c}. \end{cases} \tag{S.35}$$

Note that $\bar{\zeta}_c = \bar{v}_c^{-1}$ corresponds to the characteristic line $\bar{x} = \bar{t}$ describing the wave speed propagation. The crack solution corresponds then to the combination of a subsonic and a supersonic contribution. For Amontons-Coulomb friction, supersonic rupture speeds are in agreement with the prediction of Amundsen et al. (2015):

$$\bar{v}_c = \frac{1}{\sqrt{1 - \bar{\tau}_k^2}}, \tag{S.36}$$

which is used in Figure S3 to validate the self-similar solution against the different simulations with no free parameter. Next, the crack energy balance can be studied by inserting

the self-similar solution of Eq. (S.31) into Eqs. (12), (13), and (14):

$$E_{\text{el}} + E_{\text{kin}} = W_{\text{ext}} \tag{S.37}$$

$$\frac{1}{2}\int_0^{\bar{L}} \left(\frac{\partial \bar{u}}{\partial \bar{x}}\right)^2 d\bar{x} + \frac{1}{2}\int_0^{\bar{L}} \left(\frac{\partial \bar{u}}{\partial \bar{t}}\right)^2 d\bar{x} = \int_0^{\bar{L}} \bar{\tau}_k \bar{u} d\bar{x} \tag{S.38}$$

$$\Leftrightarrow \frac{\bar{t}^3}{2\bar{v}_c}\int_0^1 \left(\mathcal{F}'(\bar{\zeta})\right)^2 d\bar{\zeta} + \frac{\bar{t}^3 \bar{v}_c}{2}\int_0^1 \left(\mathcal{H}(\bar{\zeta})\right)^2 d\bar{\zeta} = t^3 \bar{v}_c \bar{\tau}_k \int_0^1 \mathcal{F}(\bar{\zeta}) d\bar{\zeta} \tag{S.39}$$

$$\Leftrightarrow \frac{\bar{\tau}_k^2 \bar{v}_c^2 \bar{t}^3}{6(\bar{v}_c+1)^2} + \frac{\bar{\tau}_k^2 \bar{v}_c^3 \bar{t}^3}{6(\bar{v}_c+1)^2} = \frac{\bar{\tau}_k^2 \bar{v}_c^2 \bar{t}^3}{6(\bar{v}_c+1)}. \tag{S.40}$$

Equation (S.40) is satisfied for any rupture speed $\bar{v}_c$ and at any time step $\bar{t}$ and confirms the validity of the self-similar solution of Eq. (S.31). The left-hand side of Eq. (S.40) corresponds to the mechanical energy stored in the crack that can be defined as,

$$\bar{E}_{\text{crack}} = \frac{\bar{\tau}_k^2 \bar{L}^3}{6\bar{v}_c(\bar{v}_c+1)}, \tag{S.41}$$

which is equivalent to Eq. (S.30) for slip pulse. $\bar{E}_{\text{crack}}$ corresponds to the amount of external work that is released by the rupture and converted into internal energy.

As discussed in the main text, $\bar{E}_{\text{crack}}$ can be used to derive $\bar{G}$, the fracture mechanics energy release rate (see Eq. (29)). Next, the one-dimensional dynamic fracture energy balance ($\bar{G} = \bar{G}_c$) can be used to define the crack propagation criterion:

$$\bar{d}_c \leq \frac{\bar{\tau}_k^2 \bar{x}_b^2}{\bar{v}_c(\bar{v}_c+1)} \equiv \bar{d}_c^0. \tag{S.42}$$

If satisfied, the condition Eq. (S.42) implies that the rupture releases enough energy to advance through the barrier. In practice, $\bar{d}_c^0$ systematically underestimates the fracture energy $\bar{d}_c$ required to arrest the rupture. Indeed, if the condition of Eq. (S.42) is violated, the propagating crack dissipates more energy than it releases such that rupture will arrest once the internal energy available in the 1D system is dissipated. The arrest condition should also account for the length over which the crack stops, such that the crack arrest

condition rather writes

$$\bar{d}_c > \frac{\bar{\tau}_k^2(\bar{x}_b + \bar{L}_{\rm arr})^2}{\bar{v}_c(\bar{v}_c+1)} \equiv \bar{d}_c^*. \tag{S.43}$$

In the equation above, $\bar{L}_{\rm arr}$ can be estimated as the ruptured length required for the fracture energy to dissipate the internal energy. Unlike rupture in infinite domain, the energy released by the one-dimensional rupture remains close to the interface and the internal energy is given by $\bar{E}_{\rm crack}$ defined in Eq. (S.41), such that

$$\bar{L}_{\rm arr} = \frac{\bar{\tau}_k^2\bar{x}_b^3}{3\bar{d}_c\bar{v}_c(\bar{v}_c+1)} \cong \frac{\bar{\tau}_k^2\bar{x}_b^3}{3\bar{v}_c(\bar{v}_c+1)}\frac{\bar{v}_c(\bar{v}_c+1)}{\bar{\tau}_k^2\bar{x}_b^2} = \frac{1}{3}\bar{x}_b, \tag{S.44}$$

where the last approximation corresponds to $\bar{d}_c \approx \bar{d}_c^0$. Combining equation (S.43) and (S.44) together with the relationship (S.36) between rupture speed and prestress derived by Amundsen et al. (2015), the minimal value of $\bar{d}_c$ required to arrest a steadily propagating crack corresponds then to

$$\bar{d}_c^*(\bar{\tau}_k, \bar{x}_b) = \Big(\frac{4\bar{x}_b}{3}\Big)^2(1-\bar{\tau}_k^2)\Big(1-\sqrt{1-\bar{\tau}_k^2}\Big). \tag{S.45}$$

S.4.2. Linearly decaying pre-stress

In this section, we aim to derive a solution for the final slip observed after the propagation of a crack-like rupture through decaying profile of pre-stress. Both linear decay $\bar{\tau}_k = 1 - \bar{\alpha}\bar{x}$ and quadratic decay $\bar{\tau}_k = 1 - \bar{\lambda}\bar{x}^2$ are discussed. First, we use the crack arrest conditions in absence of fracture energy ($\bar{K}(\bar{L}_{\rm arr}) = 0$) to predict the arrest position being respectively $\bar{L}_{\rm arr} = 2/\bar{\alpha}$ and $\bar{L}_{\rm arr} = \sqrt{3/\bar{\lambda}}$. Next we define the following system of coordinates $\bar{\psi} = \bar{x}/\bar{L}_{\rm arr}$ and consider the following cubic slip profile $\bar{u}_p(\bar{\psi}) = \mathcal{C}\bar{\psi}(1-\bar{\psi})^2$, which is defined to satisfy the no-slip boundary condition ($\bar{u}_p(0) = 0$) as well as zero slip ($\bar{u}_p(1) = 0$) and zero longitudinal stress ($\partial\bar{u}_p(1)/\partial\bar{\psi} = 0$) at the arrest position. The remaining constant $\mathcal{C}$ is set such that $\bar{u}_p$ satisfies the crack energy balance, which implies

that the elastic strain energy present in the system after the rupture

$$\bar{E}_{\rm el} = \frac{1}{2}\int_0^1 \left(\frac{\partial \bar{u}_p}{\partial \bar{\psi}}\right)^2 \bar{L}_{\rm arr}^{-1}\,{\rm d}\bar{\psi} = \begin{cases} \dfrac{\bar{\alpha}}{30}\mathcal{C}^2 \\ \sqrt{\dfrac{\bar{\lambda}}{3}}\dfrac{\mathcal{C}^2}{15} \end{cases} \tag{S.46}$$

corresponds to the work injected in the system by the external forces during the rupture

$$\bar{W}_{\rm ext} = \int_0^1 \bar{\tau}_k(\psi)\bar{u}_p(\psi)\bar{L}_{\rm arr}\,{\rm d}\bar{\psi} = \begin{cases} \bar{\alpha}^{-1}\dfrac{\mathcal{C}}{30} \\ \sqrt{\dfrac{3}{\bar{\lambda}}}\dfrac{\mathcal{C}}{30} \end{cases} \tag{S.47}$$

The rupture energy balance leads then to respectively $\mathcal{C} = \bar{\alpha}^{-2}$ and $\mathcal{C} = 1.5\bar{\lambda}^{-1}$ and the following slip profile

$$\frac{\bar{u}_p(\bar{\psi})}{\bar{u}_p^*} = \frac{27\psi}{4}(1-\psi)^2, \tag{S.48}$$

with the peak value of frictional slip corresponding respectively to $\bar{u}_p^* = 4\bar{\alpha}^{-2}/27$ and $\bar{u}_p^* = 2\bar{\lambda}^{-1}/9$ and being observed at one third of the total rupture length ($\bar{\psi}_{\rm max} = 1/3$). The solution (S.48) is shown by the white dashed line in Fig. 8 in comparison with simulations.

S.5. Connection with existing linear elastic fracture mechanics models

Linear elastic fracture mechanics provides an elegant and robust framework to describe the arrest of frictional rupture in lab experiments. The *small-scale yielding* assumption behind linear elastic fracture theory implies that the material behavior is everywhere linear elastic, apart from a region near the fracture tip which is of negligible size compared to any other representative length scale of the problem. The most frequent boundary conditions assumed unbounded elastic domain under constant stress, which allows for expressing the crack arrest criterion as function of the energy released at the tip of the crack per unit crack surface growth:

$$G \sim \frac{K^2}{2\mathcal{G}}. \tag{S.49}$$

G is often referred to as the *energy release rate* and is function of the stress intensity factor K that characterises the amplitude of the stress concentration near the crack tip. For example, the stress intensity factor of a mode-II crack of size L at the edge of a semi-infinite domain is given by the integration of the pre-stress (Kammer et al., 2015):

$$K(L) = \frac{2}{\sqrt{\pi L}} \int_0^L \frac{(\tau_0 - \mu_k \sigma_n)\mathcal{M}(\xi/L)}{\sqrt{1-(\xi/L)^2}} \, \mathrm{d}\xi, \tag{S.50}$$

with $\mathcal{M}(\xi/L) = 1 + 0.3(1 - (\xi/L)^{5/4})$. Using the two equations above, crack arrest is predicted as soon as the fracture energy of the interface exceeds the energy release rate:

$$G(L) \leq G_c. \tag{S.51}$$

Such dynamics is similar to the one predicted in the one-dimensional domain under stress-controlled boundary conditions. Two notable differences arise from the small-H approximation. First, the energy release rate scales as $\bar{G} \sim \bar{L}^2$ (see Eq.(29)) whereas it scales as $G \sim L$ in the unbounded domain approximation. This difference is caused by the introduction of an additional characteristic length scale (H) in the one-dimensional system. The same quadratic scaling is also observed in the energy release rate controlling the tensile delamination of double cantilever beam with similarly large aspect ratio (Anderson, 2005). Second, the tip singularity is regularized over the thickness H in the one-dimensional model, such that $\bar{K}$ does not describe the stress singularity, but rather the resultant stress at the tip, as evident in the integration of $\bar{K}(\bar{L})$ in Eq. (27), the one-dimensional equivalent of Eq. (S.50).

Another useful type of boundary conditions assumes rupture propagating between two thin-strips loaded by an imposed-displacement at the boundary (Marder, 1998; Weng &

Ampuero, 2019). In such geometry, the energy release rate rather writes:

$$G_0 = \frac{(\tau_0 - \mu_k \sigma_n)^2 H}{\mathcal{G}}. \tag{S.52}$$

Assuming small acceleration, Marder (1998) derives an approximate equation of motion for linear elastic tensile fracture in the thin-strip setup, which was recently adapted to frictional rupture by Weng and Ampuero (2019):

$$G_c = G_0\Big(1 - \frac{\dot{v}_r H}{\mathcal{A}(v_r)}\Big), \tag{S.53}$$

with v_r being the rupture speed and $\mathcal{A}$ a positive function of v_r. An important difference is that ruptures in the thin-strip geometry are pulse-like, whereas crack-like ruptures are promoted in the unbounded elastic domain. Another difference with the unbounded configuration described in Eq. (S.51) is that the thin-strip introduces some inertia in the crack equation of motion in Eq. (S.53) that stretches the arrest of the rupture over some finite arrest length. Such configuration is then equivalent to the displacement-controlled boundary conditions of the one-dimensional model. Whereas the analogy between unbounded domain and one-dimensional stressed-controlled setup was qualitative, the one-dimensional model under displacement-controlled boundary conditions directly describes the thin-strip geometry and the analogy is quantitative. For example, both in Eq. (S.53) and Eq. (21), the rupture will decelerate and ultimately arrest if

$$\frac{(\tau_0 - \mu_k \sigma_n)^2 H}{\mathcal{G}} \leq G_c. \tag{S.54}$$

Moreover, the predictions of the two models show a similar trend in the limit $\bar{d}_c \to \bar{d}_c^*$. Figure S4 compares the arrest length of one-dimensional simulations discussed in Fig. 5B of this paper to the following approximation proposed in the equation (22) of Weng and Ampuero (2019) to describe the rupture arrest observed in 2.5-dimensional earthquake

simulations, which can be written in our dimensionless formulation as:

$$\bar{L}_{\rm arr} = \frac{\alpha_s^{-0.6} - 1}{0.72(\bar{d}_c/\bar{d}_c^* - 1)}, \tag{S.55}$$

with $\alpha_s = \sqrt{1 - \bar{v}_c^2}$ defined for subsonic rupture velocity in two- and three-dimensions elastodynamics. As discussed by (Amundsen et al., 2015), one-dimensional elastodynamics promotes rupture speed which are faster than the one-dimensional wave speed (see Eq. (S.36)), which explains the large value ($\bar{v}_c = 0.975$) that should be used in Eq. (S.55) to describe the one-dimensional simulations in Fig. S4. For large $\bar{d}_c \to \bar{d}_c^*$, the small-scale yielding assumption is no longer valid such that linear elastic fracture mechanics prediction does not capture the plateau observed with the one-dimensional model.

S.6. Seismic data from 2019 Ridgecrest M_w7.1 earthquake

The data plotted in the panel (c) of Figure 9 are computed from the surface fault slip caused by the M_w7.1 Ridgecrest earthquake and inverted from optical image correlation by Chen et al. (2020). First, the strike parallel slip profile inverted from images of Sentinel-1 shown in the figure 2c of Chen et al. (2020) are digitized. Next, the non-dimensional variables $\bar{u}_p$ and $\bar{x}$ are computed respectively from the slip and the distance along strike using Table S1 (mode-II column) and assuming the following parameters: $H = 1$ [km], $\sigma_n = 200$ [MPa], $(\mu_s - \mu_k) = 0.7$ [-], $\mathcal{G} = 35$ [GPa] and the Poisson's ratio $\nu = 0.25$ [-]. As shown in Figure S5, $\bar{u}_p(\bar{x})$ is then interpolated by a cubic spline used to evaluate its second derivative and to compute $\bar{\tau}_k$ from the pulse equation Eq. (33) with $\eth$ set as 2 (negligible fracture energy).

S.7. Stress drop and back-propagating front with displacement-controlled boundary conditions ($\Gamma = 1$)

The displacement field along the interface before $\bar{u} = 0$ and after $\bar{u} = \bar{u}_p$ should satisfy the momentum equation (1) with zero acceleration. Before the rupture, this static equilibrium implies that the dimensionless stress $\bar{\tau} = 0$, which means that the frictional stress at the interface equates the initial stress in the bulk ($\bar{\tau}_f = \bar{\tau}_k$). After the rupture, the dimensionless stress becomes

$$\bar{\tau} = \bar{\tau}_k - \bar{\tau}_f = \bar{\gamma}\bar{u}_p - \frac{\partial^2 \bar{u}_p}{\partial \bar{x}^2}. \tag{S.56}$$

Moreover, one knows that the final slip should approximately satisfy the pulse equation (33), which implies that

$$\bar{\gamma}\bar{u}_p - \frac{\partial^2 \bar{u}_p}{\partial \bar{x}^2} = \eth \bar{\tau}_k. \tag{S.57}$$

Combining Eqs. (S.56-S.57), one obtains that the frictional stress at the interface after the rupture corresponds to $\bar{\tau}_f = (1 - \eth)\bar{\tau}_k$, which leads to the following stress drop:

$$\Delta\bar{\tau}_f = \eth \bar{\tau}_k. \tag{S.58}$$

For the largest admissible fracture energy (i.e. $\bar{d}_c = \bar{d}_c^*$ and therefore $\eth = 1$), the stress drop corresponds to $\Delta\bar{\tau}_f = \bar{\tau}_k$, which means that the rupture completely releases the initial shear stress ($\bar{\tau}_f = 0$). Conversely, for negligible fracture energy, $\eth = 2$ and the frictional stress after failure becomes $\bar{\tau}_f = -\bar{\tau}_k$. In dimensional unit, such overshoot can inverse the sign of the shear loading at the interface after the rupture.

If at the end of the rupture, the interface is strained with negative shear stress, it can host a secondary rupture with reverse (i.e. negative) slip and slip velocity. The same 1D pulse theory can be used to describe the propagation of this reverse secondary rupture.

First, one need to define the negative pre-stress, the equivalent of Eq.(3) but for negative slip velocity:

$$\bar{\tau}_k^-(\bar{x}) = \frac{\tau_0(\bar{x})/\sigma_n + \mu_k}{\mu_s - \mu_k} = \bar{\tau}_k(\bar{x}) + \frac{2\mu_k}{\mu_s - \mu_k} \equiv \bar{\tau}_k(\bar{x}) + \bar{\vartheta}. \tag{S.59}$$

Second, one defines the displacement due to the secondary rupture front only, $\bar{u}^- = -(\bar{u} - \bar{u}_p)$, where the minus sign is there to ensure that $\bar{u}^- > 0$. With this two ingredients, the momentum equation within the secondary rupture writes:

$$-\ddot{\bar{u}}^- = \frac{\partial^2(\bar{u}_p - \bar{u}^-)}{\partial \bar{x}^2} - \bar{\gamma}(\bar{u}_p - \bar{u}^-) + \tau_k^-, \tag{S.60}$$

which can be further simplified using Eqs. (S.57) and (S.59) into

$$\ddot{\bar{u}}^- = \frac{\partial^2 \bar{u}^-}{\partial \bar{x}^2} - \bar{\gamma}\bar{u}^- + (\eth - 1)\bar{\tau}_k - \bar{\vartheta}. \tag{S.61}$$

In the equation above both $\bar{u}^-$ and $\ddot{\bar{u}}^-$ are positive such that the theory developed in this paper to describe slip pulse can be applied to describe the dynamics of secondary slip fronts governed by Eq. (S.61). From the original one-dimensional momentum equation (1), frictional rupture are possible if $\bar{\tau}_k = 0$. Similarly, using the updated momentum equation above (S.61), secondary rupture front are possible if:

$$\bar{\tau}_k(\eth - 1) - \bar{\vartheta} > 0. \tag{S.62}$$

The equation above only guarantees that the rupture is energetically admissible. As discussed for Eq. (8), the criterion (S.62) is a necessary condition for back-propagating rupture but is not sufficient. To observe secondary rupture fronts, a local stress concentration is also required to trigger nucleation and typically arises once the main front is arrested by a sharp barrier. Figure S6 shows examples of secondary fronts nucleating at the location of a stress barrier and propagating backward following the prediction of Eq. (S.62).

References

Amundsen, D. S., Scheibert, J., Thøgersen, K., Trømborg, J., & Malthe-Sørenssen, A. (2012). 1D Model of Precursors to Frictional Stick-Slip Motion Allowing for Robust Comparison with Experiments. *Tribology Letters*, *45*(2), 357–369. doi: 10.1007/s11249-011-9894-3

Amundsen, D. S., Trømborg, J. K., Thøgersen, K., Katzav, E., Malthe-Sørenssen, A., & Scheibert, J. (2015). Steady-state propagation speed of rupture fronts along one-dimensional frictional interfaces. *Physical Review E*, *92*(3), 032406.

Anderson, T. L. (2005). *Fracture mechanics: Fundamentals and applications* (3rd ed. ed.). Boca Raton, FL: Taylor & Francis.

Bar-Sinai, Y., Spatschek, R., Brener, E. A., & Bouchbinder, E. (2013). Instabilities at frictional interfaces: Creep patches, nucleation, and rupture fronts. *Phys. Rev. E*, *88*, 060403. Retrieved from `https://link.aps.org/doi/10.1103/PhysRevE.88.060403` doi: 10.1103/PhysRevE.88.060403

Bouchbinder, E., Brener, E. A., Barel, I., & Urbakh, M. (2011). Slow cracklike dynamics at the onset of frictional sliding. *Phys. Rev. Lett.*, *107*, 235501. Retrieved from `https://link.aps.org/doi/10.1103/PhysRevLett.107.235501` doi: 10.1103/PhysRevLett.107.235501

Chen, K., Avouac, J.-P., Aati, S., Milliner, C., Zheng, F., & Shi, C. (2020, January). Cascading and pulse-like ruptures during the 2019 Ridgecrest earthquakes in the Eastern California Shear Zone. *Nature Communications*, *11*(1), 22. doi: 10.1038/s41467-019-13750-w

Courant, R., Friedrichs, K., & Lewy, H. (1928). über die partiellen Differenzengleichungen

der mathematischen Physik. *Mathematische annalen*, *100*(1), 32–74.

Cromer, A. (1981). Stable solutions using the Euler approximation. *American Journal of Physics*, *49*(5), 455–459. doi: 10.1119/1.12478

Kammer, D. S., Radiguet, M., Ampuero, J.-P., & Molinari, J.-F. (2015). Linear Elastic Fracture Mechanics Predicts the Propagation Distance of Frictional Slip. *Tribology Letters*, *57*(3), 23. doi: 10.1007/s11249-014-0451-8

Knopoff, L., & Ni, X. X. (2001). Numerical Instability at the Edge of a Dynamic Fracture. *Geophysical Journal International*, *147*(3), 1–6. doi: 10.1046/j.1365-246x .2001.01567.x

Marder, M. (1998). Adiabatic equation for cracks. *Philosophical Magazine B*, *78*(2), 203–214. doi: 10.1080/13642819808202942

Thøgersen, K., Aharonov, E., Barras, F., & Renard, F. (2021). Minimal model for the onset of slip pulses in frictional rupture. *Physical Review E*, *103*(5), 052802. doi: 10.1103/PhysRevE.103.052802

Weng, H., & Ampuero, J.-P. (2019). The Dynamics of Elongated Earthquake Ruptures. *Journal of Geophysical Research: Solid Earth*, *124*(8), 8584–8610. doi: 10.1029/ 2019JB017684

Physical quantities	Variables	Mode II rupture	Mode III rupture
Characteristic wave speed	$c = \sqrt{\frac{\Lambda}{\rho}}$	$\sqrt{\frac{\lambda + 2\mathcal{G}}{\rho}}$	$\sqrt{\frac{\mathcal{G}}{\rho}}$
Characteristic displacement	$U = H\sigma_n \frac{\mu_s - \mu_k}{\Lambda}$	$H\sigma_n \frac{\mu_s - \mu_k}{\lambda + 2\mathcal{G}}$	$H\sigma_n \frac{\mu_s - \mu_k}{\mathcal{G}}$
Characteristic time	$T = \sqrt{\frac{H^2\rho}{\Lambda}}$	$\sqrt{\frac{H^2\rho}{\lambda + 2\mathcal{G}}}$	$\sqrt{\frac{H^2\rho}{\mathcal{G}}}$
Dimensionless distance	$\bar{x}$	$x\frac{1}{H}$	$x\frac{1}{H}$
Dimensionless displacement	$\bar{u} = \frac{\langle u_i \rangle_y}{U}$	$\frac{\langle u_x \rangle_y}{U}$	$\frac{\langle u_z \rangle_y}{U}$
Dimensionless shear stress	$\bar{\tau} = \frac{T^2}{\rho U H}(\tau_0 - \tau_f)$	$\frac{\sigma^0_{xy}/\sigma_n - \tau_f/\sigma_n}{\mu_s - \mu_k}$	$\frac{\sigma^0_{yz}/\sigma_n - \tau_f/\sigma_n}{\mu_s - \mu_k}$
Dimensionless stiffness	$\bar{\gamma} = \frac{2\mathcal{G}}{\Lambda}$	$\frac{2\mathcal{G}}{\lambda + 2\mathcal{G}}$	2

Table S1. Summary of the non-dimensionalization procedure used in the present study. The elastic parameter Λ is equal to $\lambda + 2\mathcal{G}$ for Mode II rupture, and $\mathcal{G}$ for Mode III rupture.

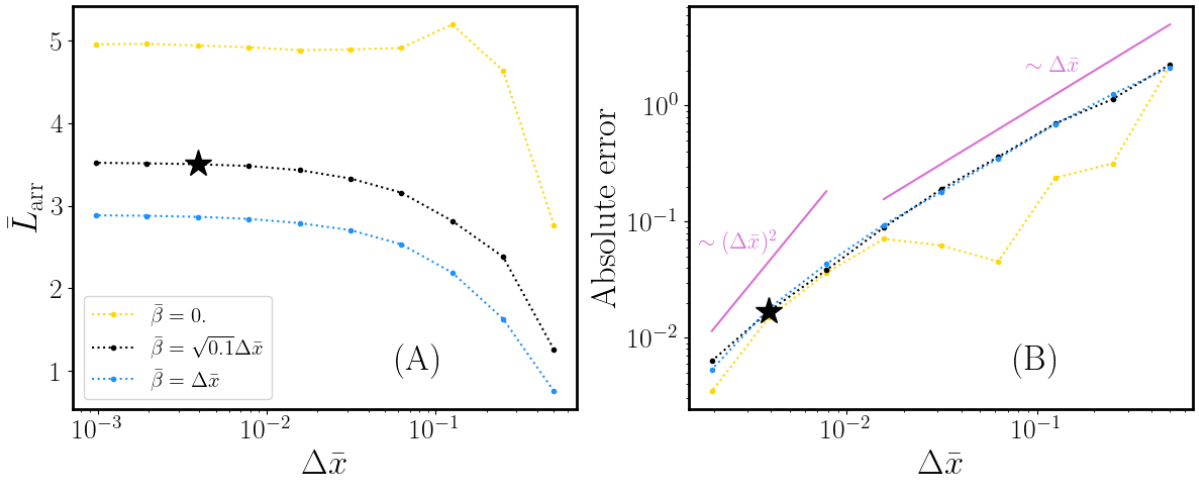

Figure S1. Convergence study of the arrest length $\bar{L}_{arr}$ for a pulse like rupture stopped by a stress barrier with $\tau_{k,0} = 0.6$ and $\tau_{k,b} = -0.3$. The black stars show the set of parameters chosen in this paper. (A) Simulated arrest length for different mesh sizes $\Delta\bar{x}$ and damping parameter $\bar{\beta}$. (B) Evolution of the absolute error (using $\bar{L}_{arr}$ for $\Delta\bar{x} = 10^{-3}$ as the reference value of each case). The purple curves show linear and quadratic convergence rates.

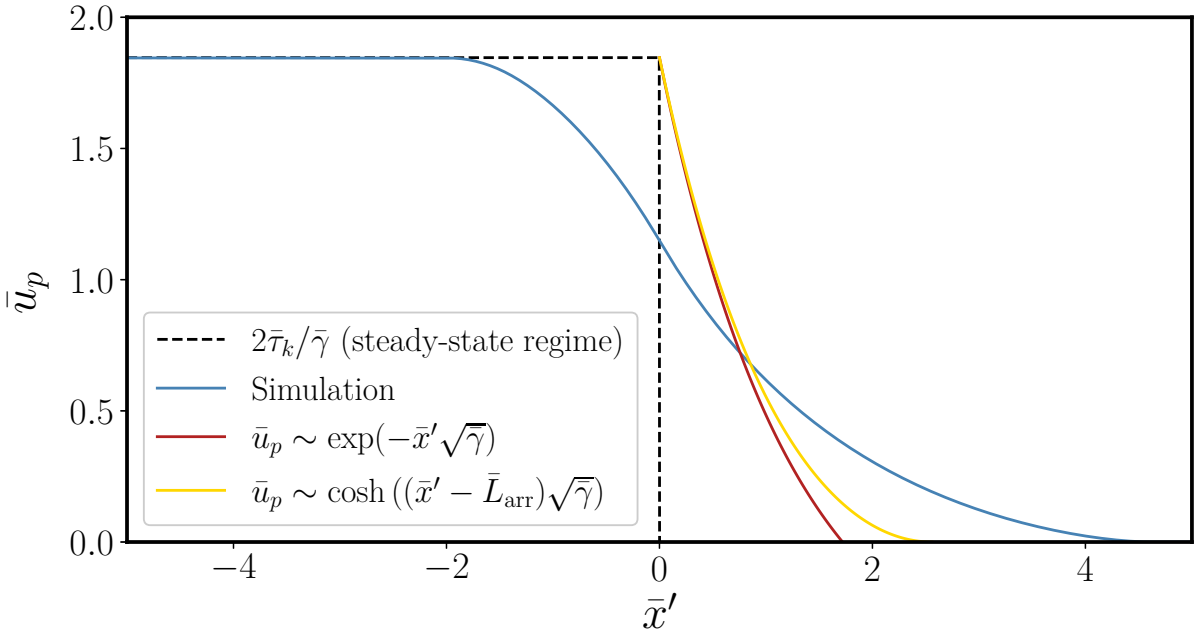

Figure S2. Decay of the final slip observed when a pulse-like rupture is arrested by a stress barrier. The simulation (blue line) is compared to two theoretical predictions derived from the pulse arrest equation (17). The red and yellow curves correspond respectively to Eq. (S.21) and (S.23).

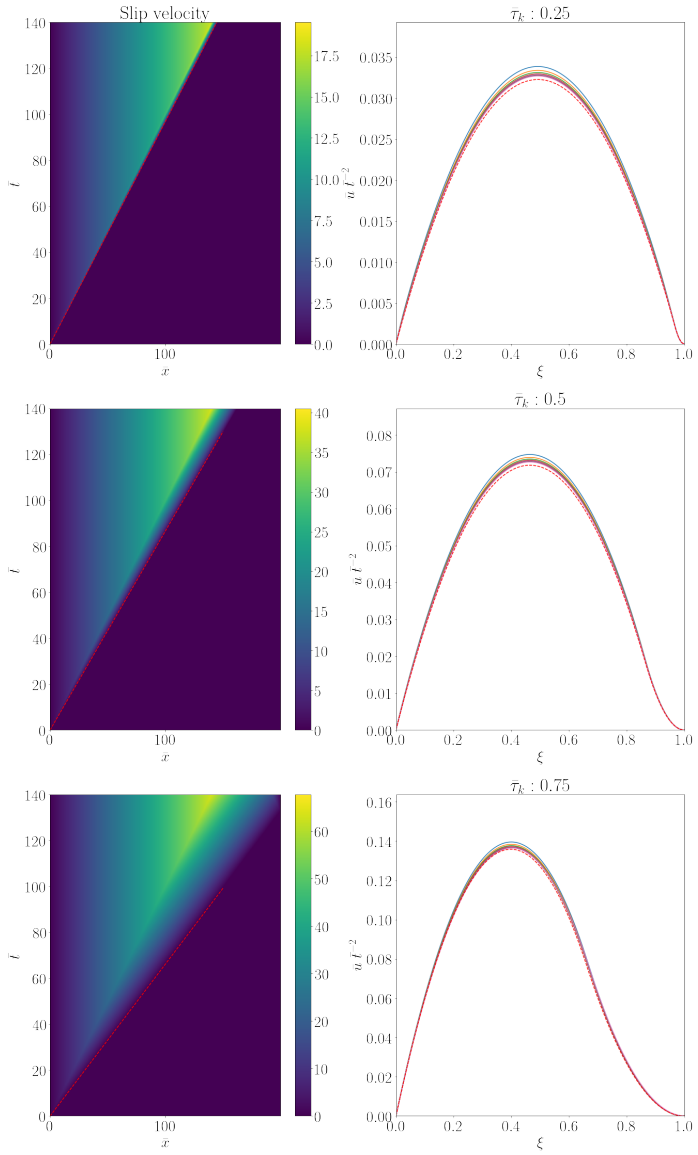

Figure S3. The three rows correspond to crack-like ruptures under three different homogeneous pre-stress $\bar{\tau}_k$ of 0.25, 0.5, and 0.75 from top to bottom. Space-time maps of the rupture are shown on the left column, with the red dashed line highlighting the steady state velocity $\bar{v}_c$ used in the theoretical predictions. The color coding shows the slip velocity. In the right column, the associated slip profile along the interface is shown at different time steps by the solid lines. Curves are collapsed by using the spatial coordinates $\bar{\zeta}$ and rescaling the slip by $\bar{t}^2$. The red dashed lines show the self-similar solution $\bar{u} = t^2\mathcal{F}(\bar{\zeta})$ according to Eq. (S.35) with no adjustable parameter.

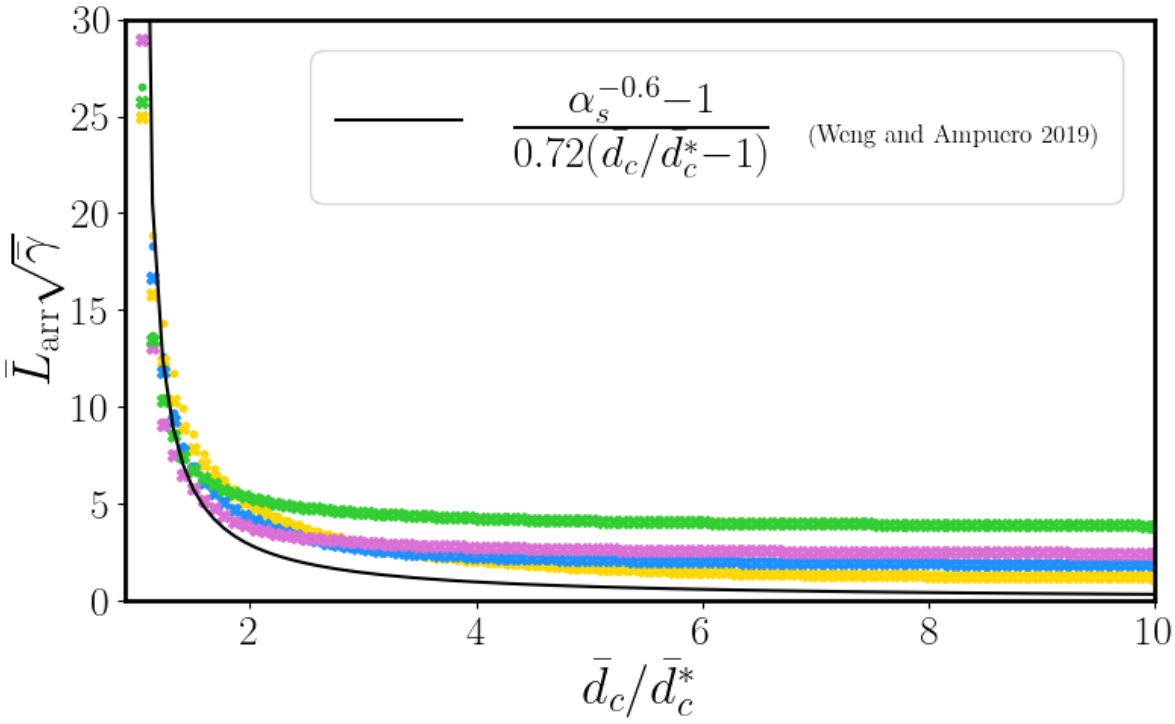

Figure S4. Evolution of the arrest length for pulse-like ruptures that arrest on a fracture energy barrier. The colored data are identical to the one displayed in Fig. 5B. The black line shows the prediction of Weng and Ampuero (2019) using Eq. (S.55) and $\bar{v}_c = 0.975$.

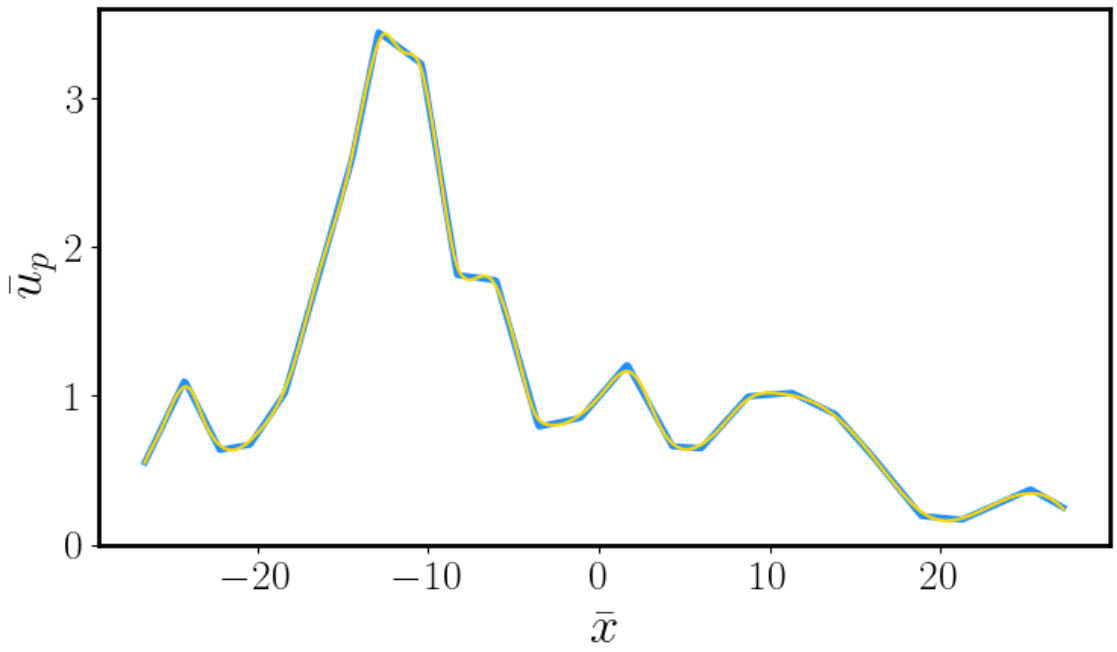

Figure S5. Dimensionless slip versus distance along the fault used to generate Fig. 9c. The blue curve shows the raw data digitized from the figure 2c of Chen et al. (2020) after non-dimensionalization. The yellow curve shows the cubic spline interpolation used to evaluate the second-order derivative of $\bar{u}_p$.

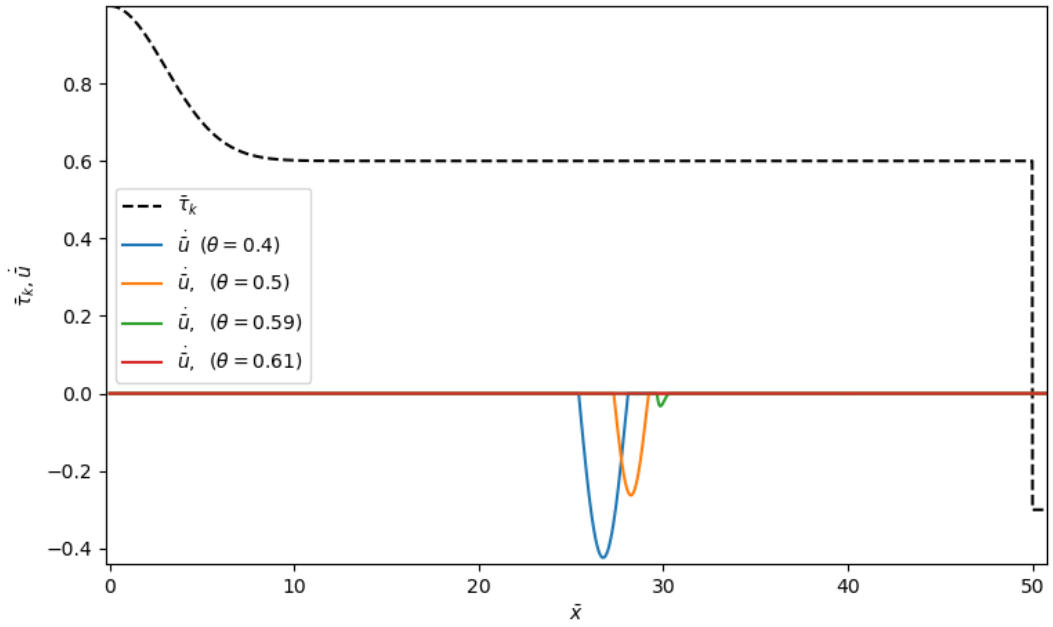

Figure S6. Secondary rupture fronts causing negative slip and propagating from the arresting barrier towards the hypocenter (a.k.a. back-propagating fronts). Snapshot are all taken at the same time step after the arrest of the main rupture front by a stress barrier. The same background stress (black dashed line) is used for the four simulations and corresponds to $\bar{\tau}_k = 0.6$ as well as $\bar{d}_c = 0$. The colored lines show the slip velocity profiles observed at the same time step after the arrest of the main front for different values of $\bar{\vartheta}$. As predicted by Eq. (S.62), back propagating fronts nucleate when $\bar{\tau}_k > \bar{\vartheta}$.